ICARUS **124,** 280–295 (1996)
ARTICLE NO. 0204

Mapping of Spectral Variations on the Surface of Mars from High Spectral Resolution Telescopic Images

ERZSÉBET MERÉNYI, ROBERT B. SINGER, AND JEFFREY S. MILLER

Lunar and Planetary Laboratory, University of Arizona, Tucson, Arizona 85721
E-mail: erzsebet@lpl.arizona.edu

Received September 2, 1994; revised March 28, 1996

We analyze a high spectral resolution ($R \simeq 200$) visible and near infrared (0.44–1.02 μm) telescopic spectral image of Mars to explore surface material variations across the observed face of the planet, which is centered on Sinus Meridiani. Two independent analysis methods are employed, linear mixture modeling and supervised spectral pattern classification with an artificial neural network. Four endmember type regions are identified with linear mixing. Further refinement is achieved with the nonlinear neural network classification algorithm, separating eight units of geological significance. Differences in spectral features among the mapped units are characterized. Among the medium- to high-albedo units northern lowlands typified by Chryse Planitia show far less evidence of bulk crystalline hematite than western Arabia or any other highland regions. The relationship of these bright units to the globally distributed aeolian dust is not yet clear. Within our image, low-albedo regions with the most pronounced crystalline hematite signature primarily correlate with the classic "dark regions," with the exception of Acidalia Planitia. Spectral evidence for pyroxenes also correlates well with most of the classic low albedo regions, but again, Acidalia Planitia is the major exception. Significant spectral anomaly is also found in an equatorial region, Deucalionis Regio. A companion paper in this issue discusses the soil properties of Deucalionis. Our data and analysis support a compositional trend that is consistent with the global geologic crustal dichotomy of Mars, namely that the younger northern lowlands contain less bulk crystalline hematite than southern highlands. © 1996 Academic Press, Inc.

1. INTRODUCTION

Visible and near-infrared reflectance spectroscopy continues to be an important tool for exploring the surface of Mars. To first order Mars appears to have a simple bimodal albedo and color distribution over a wide range of physical scales: heavily weathered red dust and soil (actually closer to orange) and relatively unoxidized dark gray rocks and sand. More detailed examination of the surface, however, with improved spectral and spatial resolution, has consistently shown increasing spectral variability and variety of surface materials, both unaltered and weathered. Mars is, after all, a large planet with a lengthy geologic history, and we should expect to see substantial mineralogic variability associated with different crustal rock types and different alteration environments. Discovering this variability has been the dominant theme of observations and interpretations by many researchers, particularly over the past decade (e.g., Singer and McCord, 1979; McCord *et al.* 1982; Bell, 1992; Clark *et al.* 1990; Singer and Miller, 1991; Pinet and Chevrel, 1990; Geissler *et al.* 1993; Murchie *et al.* 1993a, 1993b; Mustard *et al.* 1993a, 1993b). For further information the reader is referred to these papers and recent book chapters on Mars remote sensing by Soderblom (1992), Roush *et al.* (1993), and Singer and McSween (1993).

Much of the spectral variability seen on Mars is admittedly subtle. Various reasons, important to different degrees in different regions, include physical mixing of surface components, additive (checkerboard) spectral mixing resulting from limited spatial resolution, inherently weak spectral features, and relatively subtle spectral effects due to variations of a few weight % of a particular mineral (such as bulk crystalline hematite). These complications do not make the compositional variations on Mars any less real or less important, but do make them harder to investigate. Productively studying these subtle differences requires not just new and better data, which typically run into tens or hundreds of megabytes, but also increasingly sophisticated and automated analysis techniques. This paper describes and compares results of two such analysis methods (linear mixture modeling and neural network classification) applied to part of the large telescopic spectral image (hyperspectral) data set obtained by Singer and coworkers during the favorable 1988 apparition of Mars (Singer *et al.* 1990).

2. THE 1988 VISIBLE AND NEAR INFRARED TELESCOPIC SPECTRAL IMAGE

The telescopic spectral image analyzed here was acquired during the 1988 Mars opposition (07:21—08:08 UT

0019-1035/96 $18.00

26 September) using the 1.5 m telescope at the University of Arizona's Catalina Station near Tucson, Arizona (Singer *et al.* 1990). The Martian atmosphere was clear and the visibility of surface albedo units and N polar hood was excellent, as also noted by Bell (1992). Martian season was L_s 279° (southern summer), subearth latitude 21.5° S, subsolar latitude 25° S, yielding a phase angle of 3.9°. The spectral range of 0.44 μm to 1.04 μm was sampled by 300 evenly spaced channels for every spatial element. The net resolving power (R) varies from about 180 to 200. For the analyses presented here, the telluric Oxygen A band (0.75–0.77 μm) and the noisy channels longer than 1.02 μm were removed, leaving 282 spectral channels. The spatial sampling is 6.7 pixels per arc sec along the spectrograph slit (vertical), and 1.0 pixel per arc sec across the slit. During these exposures seeing was consistently better than 1 arc sec, at times as good as 0.5 arc sec. This leads to a best-case resolved footprint on Mars of approximately 280 km $\times$ 150 km. The detector was an 800 $\times$ 800 TI silicon CCD.

The data were collected as a spatial scan of individual spectrograph slit exposures. Prior to beginning this scan the instrument was rotated on the telescope to align the slit with the parallactic angle (perpendicular to the horizon). This kept differentially refracted light within the slit, to facilitate correction during the reduction procedure. The cross-slit component of differential refraction never exceeded 0.25 arc sec. The slit was stepped across the disk of Mars from W to E on the sky to provide a second dimension of spatial coverage. While the individual exposures were a fraction of a second, instrument and telescope overhead precluded scanning quickly. The 11 slit exposures in this image were collected during an approximately 45 minute period with a constant slit orientation on the sky. When these 11 slit exposures are corrected for aspect ratio and aligned side-by-side, an *approximate* orthographic view of Mars results, as shown in Fig. 1. This view differs from a true orthographic map because of rotation of the planet between exposures and slight errors in slit placement due to image motion at the telescope; therefore it should be used for spatial interpretations only with due caution. Nevertheless, prominent albedo features are readily identifiable in this view, with Sinus Meridiani (low-albedo) near the center. All the pixels within a given spectrograph slit are highly consistent, since they were obtained at all wavelengths at the same instant. The calibration between slit exposures is also good, but slight differences do appear due to the time difference between slit exposures and consequent small changes in the Earth's atmosphere. Additional contributions to the observed differences might also include variations in the Martian atmosphere and/or photometric effects as the slit was translated and Mars rotated. There is also a visual illusion, especially when looking at the approximate orthographic view of the data, that regions straddling a slit boundary appear different on each side. As explained, the orthographic view is at best only approximately correct, because of image motion and variations in slit location from what was planned. In most cases the apparent inconsistencies are due to gaps or overlaps between adjacent slits exposures. To facilitate more accurate spatial correlation among spectra a procedure of transforming individual slit exposures to a cylindrical map base was developed by Pierazzo and Singer (1993). This method generally places features within a few degrees of their location on standard Viking-based maps, given standard observational uncertainties.

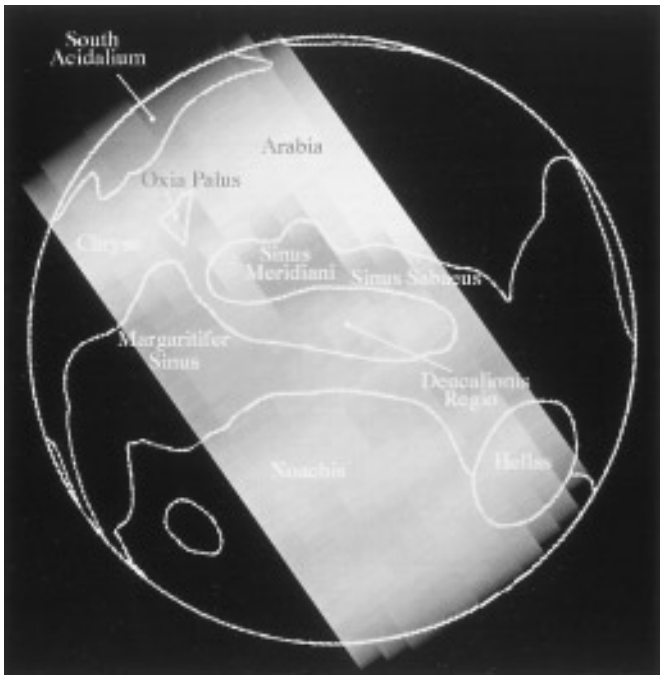

FIG. 1. The September 26, 1988 telescopic view of Mars. Shown here, the 0.75 μm band was selected from the 300 bands of the spectral image to illustrate the main albedo features. The image is in approximate orthographic view, centered south of Sinus Meridiani. Outlines of surface albedo units are superimposed.

The data values of Mars spectral reflectance analyzed in this paper are Mars/HD 1835, where HD 1835 is 9 Ceti, a G2V solar-analog star. The values differ from Radiance Factor (Hapke and Wells 1981) by a constant multiplicative factor; the zero level is accurate. Spectral flux observations of HD 1835 were obtained through courtesy of Lockwood and Thompson (unpublished, Lowell Observatory). Additional observations conducted by us in 1990 spectrophotometrically compared HD1835, 16 Cygni B and HD 28099, which is another well accepted solar-type star. We found the agreement among the spectra of these stars to be very good. The differences among the calibrated results using these three standard stars were less than 3.5% in any channel. A wide (6 arc sec) slit was used to capture star light in order to assure good photometric accuracy. Widening

the slit inherently lowers the spectral resolution. To correct for this, the wide slit star observations were combined with a high-pass filtered 1 arc sec slit star image, producing an image with correct flux and with spectral resolution matching the Mars slit images. After considerable development and testing we have found this technique to produce excellent spectrophotometric accuracy. Data reduction was largely done using the IRAF astronomical software package from the National Optical Astronomy Observatories (Tody 1986). Reduction included bias and flat field correction. CCD bias (dark) observations were made frequently throughout the night to account for drifts in overall bias level due to various sources. After all observations were completed, however, we found that using a single bias near in time (or two bracketing a set of exposures) appeared to visibly increase the pixel-to-pixel noise more than correcting with an averaged bias. For this reason, an average CCD bias level was computed for the night and scaled to the level of the bias nearest in time to a set of star or Mars observations to improve the correction. Individual flat fields were collected each time the telescope was moved to observe a new object, to allow for possible effects of mechanical flexure. A low-order color curve was divided from the flat fields to remove the effect of color variations in the flat field lamps (due to warm-up and aging) but preserve CCD pixel-to-pixel gain differences. This processing technique has also proven very effective. CCD flaws and cosmic ray hits were removed and averaged over. Each standard star and Mars image was divided by exposure time (varying with object brightness to give best S/N without saturation) to normalize DN to flux per unit time. Differential refraction effects were removed by computing a function for star brightness peak displacement as a function of wavelength, then transforming the image to straighten the curve. Mars images were refraction-corrected using a star image of matching air mass. To correct for terrestrial atmospheric extinction, we used HD 4628 (K5V, near Mars in the sky) as an extinction standard, observing it several times per night at air masses ranging from near 1.0 to near 2.0. A model extinction curve for each night was developed for air masses between 1.01 and 2.00 at 0.01 AM intervals by interpolating the logarithms of the HD 4628 spectra. This procedure assumes Beer's Law absorption (unsaturated absorption lines) which is not strictly true for oxygen and water bands, but nevertheless produces good results to the 1–2% level. Because there was significant variability in extinction during this night, the atmospheric standard star spectrum nearest to our Mars observations was used rather than the results of extinction analysis. CCD exposures of a mercury–argon lamp were used to calibrate the nonlinear prism dispersion of the spectrograph and transform them to a consistent linear dispersion of 0.002 μm per spectral channel. Multiple sets of extinction-corrected solar standard spectra were averaged together to provide a dependable ratio of HD 1835/HD 4628. This average spectrum was applied to the Mars exposures to produce Mars/HD 1835, differing by a constant from Radiance Factor. The reduced Mars slit images were then aligned to center them at the same spatial channel, and assembled to form image cubes, with dimensions similar to an orthographic view of Mars. These data and the calibration procedures are described further by Singer *et al.* (1990) and Miller *et al.* (1992).

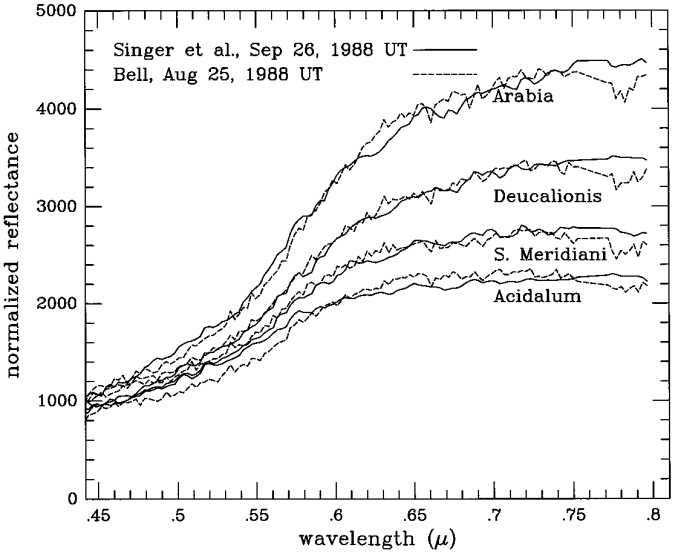

FIG. 2. Comparison of 1988 telescopic data sets. Solid lines are from data taken by Singer *et al.* September 26, 1988 UT; dashed lines are from Bell's image cube 849, taken August 25, 1988 UT. To make the comparison, our data set was first resampled to the somewhat lower spectral resolution of Bell's data and then both image cubes were brightness normalized as described in Section 3.2, to allow direct comparison of the spectral characteristics.

Our data agree well with previous and near-concurrent observations of Mars (cf., McCord *et al.* 1977; Bell *et al.* 1992; Pinet and Chevrel 1990). The agreement with Bell's telescopic spectral image cube 849, which was taken one month earlier than ours, is within a few percent of the data range, as shown in Fig. 2. This comparison also indicates a signal-to-noise ratio similar to that of Bell's data (Bell *et al.* 1992). A slight systematic difference between our data and similar data sets occurs in slopes of the near-IR end of the spectra (between about 0.9 and 1.02 μm). Whatever the source of this difference it should be stressed that it does not affect our mineralogic interpretations (e.g., pyroxenes), which are in good agreement with those from other sources (e.g., Singer and McSween 1993).

This data set is unique in that this is the only spectroscopic imaging of Mars in 1988 that provides continuous wavelength coverage of the given geographic areas over 0.4–1.02 μm. Several of the image cubes that Bell *et al.* (1992) recorded at about the same time are centered on

Meridiani Sinus but have spectral information only to 0.8 μm. Pinet and Chevrel (1990) took CCD measurements centered on Syrtis Major in nine selected bandpasses, mostly beyond 0.9 μm. As seen from the next sections, this difference in the wavelength coverage is important for one of our most interesting analysis results.

3. SPECTRAL ANALYSES

Two independent analyses of these data are presented here, linear spectral mixing and supervised classification with an artificial neural network, which show significant spectral variability.

This image has been analyzed earlier by Singer and Miller (1991), Miller and Singer (1993), Pierazzo and Singer (1993), and Singer *et al.* (1993). Figure 3 shows examples of two such previous analyses. Figure 3.a is a spectral band depth map for the 0.86 μm hematite band, while Fig. 3b is a spectral band depth map for pyroxene bands between 0.9 and 1.0 μm. Regions with the most pronounced crystalline hematite signature spatially correlate primarily with the classic low albedo units such as Sinus Meridiani and Sinus Margaritifer. The most notable exception is Acidalia Planitia, which is relatively poor in crystalline hematite (based on the 0.86 μm band, at least). The pyroxene distribution, as mapped by the depth of Fe^{2+} crystal field absorptions centered between 0.9 and 1.0 μm, also correlates well with most of the classic low albedo units. Again, Acidalia Planitia is an exception, showing less evidence for crystalline pyroxene content than even the weathered bright region Arabia. Some of these results were unexpected when first observed. They are corroborated by the new analyses presented here, which map the occurrences of several spectral types simultaneously. The linear mixture model separated four distinct spectral types, and the artificial neural network was able to distinguish eight different spectral classes with geological meaning. To facilitate spatial comparison with both earlier analyses on the same data and with standard Viking maps, we present details of our analyses in the original spatial arrangement and show final results projected in a cylindrical map base.

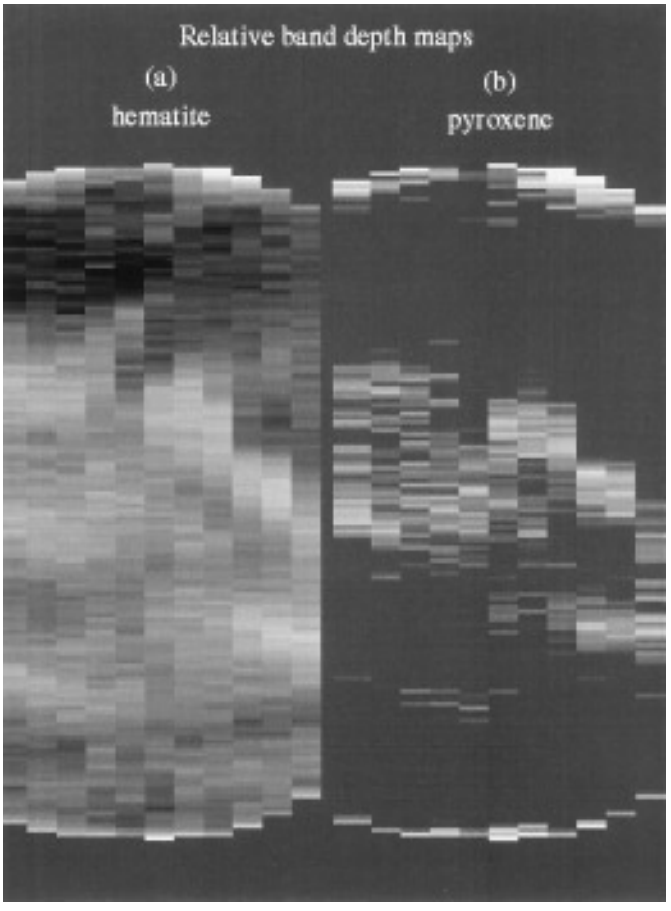

FIG. 3. Image orientation is as shown in Fig. 1: (a) A 0.86 μm hematite band depth map from ratioed spectral image data. Black regions show the least and white regions the most spectral evidence for bulk crystalline hematite. The grey scale represents a range of −2–6% for this absorption feature, from black (−2%) to white (6%). This image was prepared by dividing the spectral image by an averaged spectrum taken from the southern end of the dark region Acidalium (to accentuate the 0.86 μm band) and fitting the spectrum from 0.75–0.95 μm with a cubic polynomial, then drawing a straight-line continuum between 0.75 and 0.95 μm. The band depth was determined according to the following formula: $BandDepth = 1 - \text{Reflectance}_{\text{bandminimum}}/\text{Reflectance}_{\text{continuum}}$. (b) Band depth map for the 0.9–1.0 μm pyroxene band. Lighter shades indicate deeper bands, with white corresponding to about 10% band depth. Areas with no obvious pyroxene absorption have been masked out to the background gray. The brightness of the north and south limbs is an artifact and should be disregarded. Polynomial fitting was done on reflectance data rather than on ratio data (as in the previous case). Band depth was determined using the same formula as for 3(a). Refer to Miller and Singer (1993) for discussion of details and assumptions in this analysis.

3.1. Linear Mixture Modeling

Linear mixture modeling seeks to find the best linear combination of given endmembers for each pixel in a spectral image (e.g., Adams *et al.* 1986). The endmember spectra are picked from the image itself, and thus represent the various spectral types in the scene. The image endmember selection is based primarily on the spectral extremes of the modeled area. The selection of the endmember candidates is guided by known geologic varieties within the scene. One usually starts by picking two or three endmember candidates and calculating, for each pixel, the fractional contributions of the selected endmembers and the residuals for all channels, by solving an equation system of the form

$$Y_b = \sum_{i=1}^{NE} f_i \cdot X_{b,i} + r_b \quad b = 1, \ldots, NB \tag{1}$$

with the constraint

$$\sum_{i=1}^{NE} f_i = 1 \qquad (1.1)$$

so that $\sum_{b=1}^{NB} r_b^2$ is minimum, where Y_b is the DN (data number) of the given observed pixel in band b, $X_{b,i}$ is the DN of the ith image endmember for band b, f_i denotes the unknown fraction of the ith image endmember, and r_b represents the residual error for band b. NE and NB are the number of image endmembers and bands, respectively. $NE < NB$ must hold, otherwise (1) would be underdetermined. Since in our case $NB = 282$ and the intrinsic dimensionality of the data is much less than that, this latter constraint is automatically fulfilled. The residuals and the total error—the Euclidean distance between the data vector and the model—are calculated for each pixel and indicate which parts of the scene are poorly modeled by the given set of endmembers. Then, the endmember set is improved by replacement with spectrally more extreme pixels and/or by adding another one from a poorly modeled area, and the whole fraction calculation is repeated. This iteration continues until the model fit is acceptable: errors become low (comparable with the noise level), and the fractions have physically meaningful values (mostly between 0 and 1). Recently, considerable efforts have been made to automate the determination of the spectral extremes (e.g., Tompkins *et al.* 1993; Boardman 1993). In this approach, pixels are modeled independently, and the spatial coherence of the similar fraction values in the resulting endmember fraction images can be used to support geological context. In the visible and near-infrared range, this technique has been used by a number of researchers in a variety of geological studies (e.g., Adams *et al.* 1986; Smith *et al.* 1990; Blount *et al.* 1990; Farrand and Singer 1991; Mustard 1993; Pinet *et al.* 1993).

Earlier applications typically dealt with 0.1–40 m/pixel (e.g., for Earth remote sensing and Viking Lander images) to about 1 km/pixel (Viking Orbiter pictures, for example, e.g., Head *et al.* 1992). Compared to that, our image has a very large spatial scale, 280 × 150 km/pixel at best. This presents additional numerical limitations indirectly. Due to integration over large spatial areas, the angular distance between any two vectors (spectra) in our image is typically half as big as that, for example, in a high spatial resolution (10–20 m/pixel) image of a terrestrial site. Similar spectra in this scene therefore produce linearly dependent vectors easier and can cause linear inversion algorithms to break down. Bell (1992) also notes such difficulties in the mixture model analysis of his very similar data set (Bell *et al.* 1992).

Shade was also always used as an endmember, as advocated by Adams and co-workers. Shading effects at these large spatial scales are mainly albedo variations and limb darkening, corresponding to the fact that at our spatial scale the pixel-to-pixel variation of shade is smaller than in images of high spatial resolution. The primary reason for this is that shadows are far smaller than our pixel size. Indeed, the shade fraction image became quite featureless showing only a pattern of the major albedo units and darkened limbs, as we were improving on the model fit by the inclusion of additional spectral endmembers. In the final model it maps the major albedo units with nearly constant values within units.

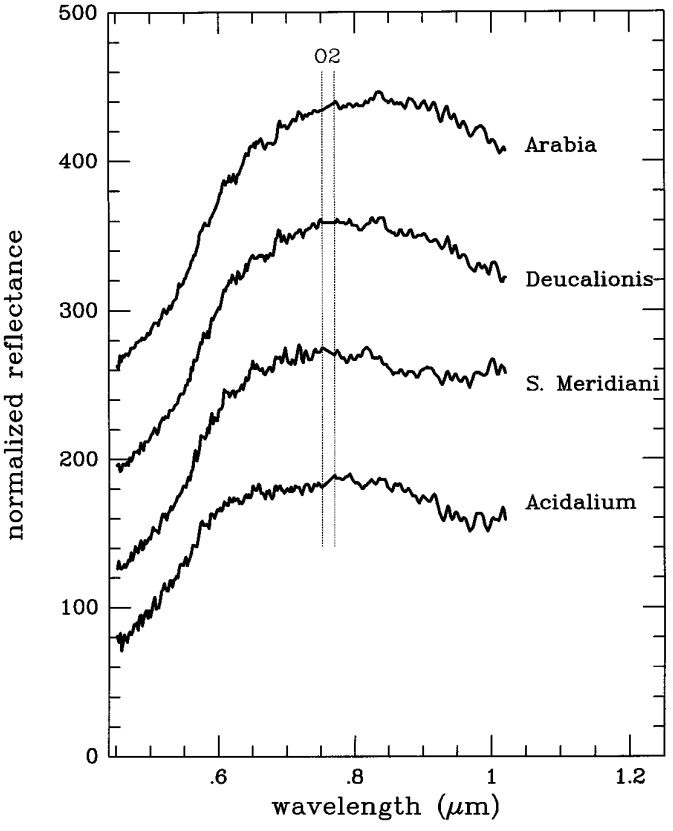

FIG. 4. Endmember spectra for the linear mixture model, selected from type regions of Arabia, Deucalionis Regio, Sinus Meridiani, and South Acidalium. Curves are offset for viewing convenience. The *y*-axis units are arbitrary.

In our 1988 spectral image of Mars, initial choices for endmember spectra were determined from examination and comparison of spectra extracted from different major regions: from Western Arabia, South Acidalium and Sinus Meridiani (Fig. 4). Figure 5 is a mosaic of four different mixing trials for our data, with Fig. 5a being the final, best model. As seen in Fig. 5b, the model based on the above three endmembers fits the scene well, except for large errors in the Deucalionis Regio area and, to a lesser extent, in Chryse/Xanthe, Oxia, and Noachis. Deucalionis Regio is indicated in Fig. 1. Its main body extends from 330°W to 10°W across the prime meridian and between 13°S and 17°S. The western end curves to the northwest at a nearly right-angle toward Oxia Palus to form the southern and western borders of Sinus Meridiani (Antoniadi 1930). The

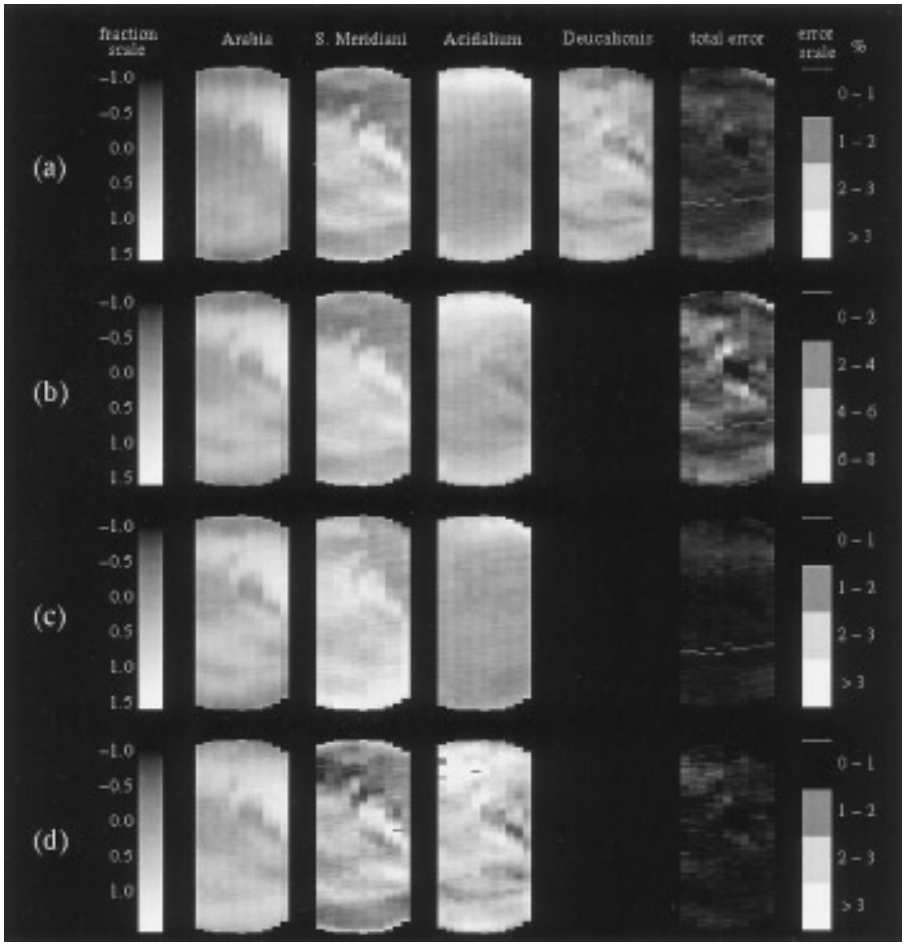

FIG. 5. Results of mixing modeling. Shown are image endmember fractions and the total error for several models. Higher intensity means more contribution of the respective endmember to the given pixel. The total error is given relative to the data, i.e., percentage of the magnitude of the data vector. (a) Image endmember fractions and the total error of the best linear mixture for our 1988 telescopic image cube. Endmember spectra in this model represent type regions Arabia, Sinus Meridiani, South Acidalium and Deucalionis Regio. All image fractions fall between 0 and 1 within noise level. The total error is within 2% except for the condensates near the upper right edge of the disk. As the endmember vectors approach linear dependency, finer differentiation may not be possible with linear inversion. For example, the condensates over the north polar hood, shown by the brightest pixels on the error image in (b) close to the north limb, could not be separated from Acidalium with mixture modeling. The inclusion of both an Acidalium and a ''condensate'' endmember resulted in numerical problems. (b) A mosaic of three endmember fraction images and total error. Endmember spectra in this model represent type regions Arabia, South Acidalium, and Sinus Meridiani. Deucalionis Regio, marked by the brightest pixels to the south and to the NW of Sinus Meridiani, was brought to our attention by the error image of this three-endmember model. Here, Deucalionis shows the largest error, about 7% at maximum. (c) Same as (b), with the mixing modeling done only for the 0.4–0.8 μm region. No error shows in the Deucalionis area, suggesting that the spectral distinction for that region is mostly beyond 0.8 μm. (d) Same as (c), for the 0.8–1.02 μm spectral range. Errors show in Deucalionis Regio, along with Chryse and Noachis.

part of Noachis seen in our image extends roughly between 20°W and 340°W and between 30°S and 50°S. Selection of an additional endmember spectrum from Deucalionis (15°S, 345°W) resulted in a model fit within 5% residual error for all pixels with 1.1% mean absolute residual and 1.5% standard deviation across pixels and with endmember fractions between 0 and 1 within the noise limit (Fig. 5a). Other likely endmember combinations, with spectra from major albedo units such as Margaritifer Sinus, Hellas, Chryse, and Oxia Palus, have produced poorer model fits. Fewer than three image endmembers (a classic dark and bright spectrum, for example) were clearly inadequately modeling this image. An independent principal components analysis showed that at least four image endmembers were needed to span out this data space. Our attempt to model the optically thin condensates over the north polar hood by including a ''cloud'' endmember with the above four was unsuccessful, due to the strong similarity between the cloud and the Acidalium endmember spectrum over our entire wavelength range. This is not surprising since

the polar hood clouds are optically thin, and therefore spectrally mix in a nonlinear way. Residual image analysis, however, reveals the condensate locations, and as seen from the neural net classification (Section 3.2), clouds are directly distinguishable with a non-linear pattern recognition method.

The best model in Fig. 5a indicates a spatial distribution of the Sinus Meridiani type endmember very similar to that of the strongest 0.86 μm band signatures in Fig. 3a. This is consistent with earlier interpretations, as discussed above.

The interesting finding in this analysis is the strong spectral anomaly for Deucalionis Regio. As shown in Fig. 5a, Deucalionis Regio is well distinguished from the other regions, and the same ''Deucalionis material'' is also found in smaller concentrations in Oxia, Chryse, and Noachis.

Detailed residual analysis from linear mixture modeling also suggested that in this image Deucalionis Regio is most unique in the 0.8–1.0 μm range. This was further confirmed by running the mixing model with the Arabia, Acidalium, and Sinus Meridiani endmembers on just the 0.4–0.8 μm interval, which resulted in a good fit, with no appreciable error showing in the Deucalionis region (Fig. 5c) while the mixture model of the same three endmembers in the 0.8–1.0 μm region did generate errors for Deucalionis Regio (Fig. 5d).

Quantitative examination of the Deucalionis endmember shows over 50% contribution in Oxia, Chryse, and Noachis. Noachis in particular seems to be a contiguous area of uniformly high Deucalionis fractions. A follow-up investigation (Merényi *et al.* 1993a, 1996) revealed that both the compositional and the physical properties of the soil in Deucalionis are significantly different from those of the nearby surface units and that the same or very similar properties can be seen in Noachis.

3.2. Artificial Neural Network Classification of Spectra

Supervised classification of the spectral shapes with an artificial neural network was done for the same image. A comprehensive review of artificial neural networks (ANNs) can be found, e.g., in Pao (1989). The increasing use of ANN's for pattern recognition and classification over the past 5–10 years has been motivated, beyond their sheer computing speed, by the quality of their performance and by their ability to model complex shapes without analytical description. They have proved to produce equal or higher quality classification results than conventional classifiers (e.g., Huang and Lippman 1987), while being more tolerant to noise. Specifically, the power of artificial neural networks in dealing with complicated patterns such as noisy geological spectra has been demonstrated by several works in the remote sensing field (e.g., Hepner *et al.* 1990; Ninomiya and Sato 1990; Benedikttson *et al.* 1990; Ryan *et al.* 1991; Merényi *et al.* 1993b). There have been numerous ANN paradigms developed for various kinds of problems.

The neural network paradigm we used here is a Kohonen self-organizing map (Kohonen 1988) combined with a categorization learning output layer (implementation by NeuralWare, Inc., 1991). For background and details on this particular ANN construct see Howell *et al.* (1994). As is true of neural nets in general, it is a densely interconnected set of processing units organized into different functional groups. There are an input layer where data are introduced, one or more hidden layers to process the data, and one output layer where class predictions are represented. The system is a learning machine that derives its knowledge from examples shown to it many times. In this case the selected spectral types that we want to map, together with their class designations, make up the training material. The network is trained until it correctly classifies all training samples. Then it is asked to make a class prediction for each pixel of the spectral image.

For this work we used a network configuration with one input, one hidden, and one output layer. Each of 92 input processing units received an average over three spectral channels. The 10 output units corresponded to our 10 spectral classes. The hidden layer consisted of a 20-by-20 2-dimensional Self-Organizing Map (Kohonen 1988). Prior to classification, the spectra were normalized for brightness: instead of spectrum $S = (s_1, \ldots, s_n)$, $S^* = S/norm(S)$ was used, where $norm(S)$ is the Euclidean vector norm of spectrum S, $norm(S)^2 = \sum_{b=1}^{NB} s_b^2$.The geometrical interpretation is that the magnitude of the vector is scaled to unity while the directions to the coordinate axes—the spectral properties—are preserved. This treatment cancels the illumination geometry effects and shading effects and it also eliminates albedo differences; thus the spectral characteristics can be compared directly.

Ten different spectral units have been used for supervised classification, including the types that served as endmembers in the mixture model analysis. The classification was performed on two differently preprocessed versions of the spectral image. One is the original form, with brightness normalization as described above. The bottom row of Fig. 6 shows one representative training spectrum in this form for each class. Typically, 5–10 training spectra were used per class. First, however, we ratioed the whole image cube to an Acidalium spectrum in order to enhance the subtle relative differences among the spectra. This mainly emphasizes the differences in the Fe^{2+} and Fe^{3+} absorption features relative to Acidalium and helps the human eye see the spectral varieties more easily (Fig. 6, top row). Looking at the data in this form, we could select ten different spectral types for training. Eight of these have geologic interpretations as discussed later. The remaining two classes that we used for training represent the limb effects and

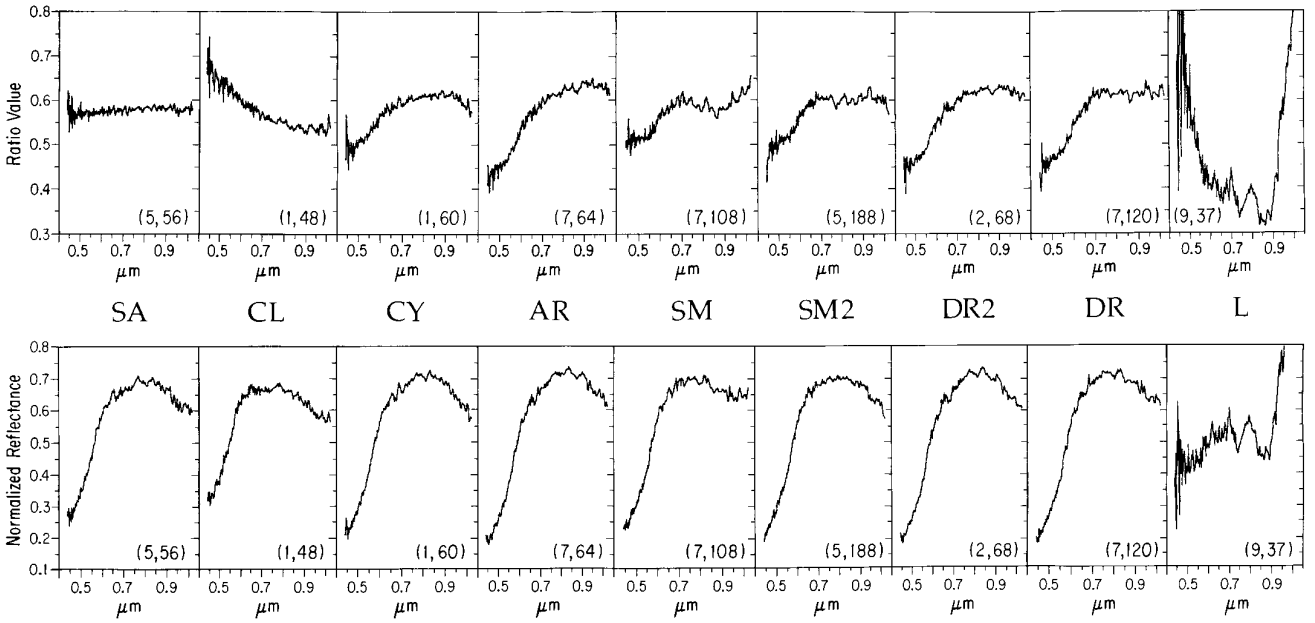

FIG. 6. Training spectra for the supervised neural network classification. These two rows of spectra represent two sets of training data that were used for neural network training, in two separate runs. Each spectrum is a representative of a small (5–10 member) training set, and is labeled by the image cube (x, y) coordinates the spectrum was taken from. The acronyms between the two rows identify the spectral type regions as follows: SA = Acidalia Planitia; CL = optically thin atmospheric condensates; CY = Chryse; AR = Arabia; SM = hematite rich soil 1; SM2 = hematite rich soil 2; DR = Deucalionis Regio 1; DR2 = Deucalionis Regio 2. The three remaining classes have no geological relevance: U = unclassified; L = limb effects; and S = sky/background. The units on the y axes are arbitrary. The spectral properties are discussed and interpreted in Tables I and II. The spectra in the top row are ratios of the original ones to the same Acidalium spectrum (5,56), to enhance the differences in the 0.7–1.0 μm region. The data were used in this form for the band depth mapping (Fig. 3); therefore the neural network was given this sample set to get a comparision with the 0.86 μm band depth map. The classification results from this training are presented in Fig. 7.a. The spectra in the bottom row are brightness normalized as described in Section 3.2. These were used in the neural network training that produced the classification shown on Fig. 7.b. Using this form gives a fair comparision with the mixing modeling results (Figs. 5 and 8).

sky background. Training pixels for each class were picked so that they represent the spectral variations within the class as much as possible. Consequently, some of the classes are broader or ''tighter'' than others (the standard deviation varies from class to class).

In Fig. 7a, the color-coded units show the classes which were identified by the neural network, allowing further distinction among the spectral types compared to the linear mixing model. This map provides a fair numerical comparison to the band-depth mapping (Fig. 3), as the spectra were used for the latter in the same ratioed form. We then ran the neural net classification on the original, brightness normalized spectra, using for training the equivalent samples from the same locations (Fig. 6, bottom row). The resulting map (Fig. 7b) indicates that the neural network is as sensitive to the spectral differences in this form as in the divided spectra. As the signal-to-noise ratio is lower in the divided spectra, misclassification is more likely to occur. In Fig. 7a, the blue area near the bottom of the map contains pixels misclassified for ''Acidalium type,'' whereas the same area appears as unclassified in Fig. 7b. The latter prediction is more accurate. Visual observation and simple statistical comparison of the spectral patterns in question verifies that they are different from SA spectra and represent a continuous change-over from SA to scattered light (limb) spectra. Other differences between the maps in 7a and 7b are similarly attributable to the fact that the source data for 7a are noisier, which makes 7a a less reliable map than 7b. Detailed comparison of the training spectra and the spectra of the respective predicted classes clearly show a closer match for 7b as explained below. The highest level of confidence in the mapping should be placed in regions where the two figures agree, which is in large areas of Arabia, South Acidalium, SM and DR. The more reliable map of the two, 7b, was used for further evaluation of the spectral properties of the classes. We emphasize here that the different classes refer to spectral types, not strictly to geographical units. For example, the ''Chryse class'' maps the occurrence of spectra similar to the training spectra for this class, taken from the middle of the Chryse basin (40° W, 17° N).

Figure 8 is a color display of the mixing model results in Fig. 5.a and the ANN classification in Fig. 7b, projected in cylindrical map base. Lacking ''ground truth,'' we assess

TABLE I
Comparison of Spectral Units

r_F		VIS slope		0.55 μm		0.6–0.7 μm		0.86 μm		0.9–1.0 μm	
Bright	Dark	Bright	Dark	Bright	Dark	Bright	Dark	Bright	Dark	Bright	Dark
AR (.42)	CY (.36)	AR	SM2	DR	SM2	CY	SA	DR	SM	DR	SA
DR2 (.39)	SM2 (.33)	DR[a]	CY[a]	DR2[a]	SM[a]	AR[a]	CY[a]	AR	SM2	AR[a]	SM
DR (.37)	SM (.31)	DR2[a]	SM[a]	AR[a]	CY[a]	DR[a]	SM2	DR2[a]	SA	DR2[a]	SM2[b]
CY (.36)	SA (.28)	CY	SA	CY	SA	DR2[a]	SM	CY[a]	CY	CY	CY[b]

[a] Regions within the same column are very similar.
[b] Comparable to SA at around 0.95 μm.

the goodness of the classification as presented in Fig. 9. The mean of the training spectra is compared with the mean of the predicted class for each geologic type. The standard deviation within the class is also plotted for all channels. The two means are very close in all cases, and virtually identical for several classes with small standard deviations, which is a measure of the pattern recognition quality. In addition, we have also checked how the envelope (the two curves defined by the channel minima and maxima) of a predicted class compares to the envelope of the training spectra of the same class. It is interesting to point out that the Deucalionis class (DR) is the tightest of all in terms of matching means and very small deviations. This indicates spectral homogeneity over Deucalionis and the part of Noachis that is included in our image.

Comparison with Figs. 5a, 8a, and 8b shows that the spectral types used in the linear mixture model (Arabia, Sinus Meridiani, Acidalium and Deucalionis Regio) are mapped similarly by the neural network classification. However, while the linear mixture model gives fractional contributions, the classification map assigns the most probable class to each pixel. Pixels of intermediate colors in the mixture model (Fig. 8a) indicate contributions from more than one endmember, while pixels of grey color on the classification map indicate spectra about which no firm class membership decision could be made based on the training spectra. Compared with the mixture model, further subdivisions were found in the classification map within the Sinus Meridiani and Deucalionis Regio types. The two subclasses of Deucalionis, DR and DR2 (green and dark green on the map), are conspicuously separated by latitude. These two classes are both very tight (i.e., the standard deviation is small for each class) even though DR extends over a large area, and they are too similar for the linear mixing model to separate them. Still, there is a consistent and real spectral difference between them, which is detected by the nonlinear pattern recognition method.

Optically thin condensates have also been separated easily within Acidalium by the network, despite of just a slight difference compared to Acidalium type spectra at the initial segment of the blue wavelength range (Fig. 9). The spatial and spectral coherence of the unclassified pixels suggests that further geologically meaningful variety may be present.

4. DISCUSSION OF THE SPECTRAL UNITS

4.1. Spectral Variations among the Mapped Units

Representative spectral shapes for the units that were mapped (Figs. 7 and 8) can be seen in Fig. 6. Because the spectra were normalized for brightness (as noted above), we can readily compare their spectral properties. Interpretation is based on broad spectral features and continuum shapes, while small, high-frequency variations (1–5 channel features due to noise and residual atmospheric and stellar lines) are disregarded. These spectra exhibit subtle but real differences on the order of a few percent of the data value range, which are enhanced in ratios and are important for their interpretation. By using class averages in ratios, noise is sufficiently reduced to reveal features that may otherwise remain hidden. We ratioed every class mean (Fig. 9) to all others and intercompared and ranked the spectral units according to the strengths of several key spectral features listed in Table I. Based on that we present below a discussion of spectral differences among the seven major units. The results are summarized in Table I. Due to the large number of the pairwise ratios, we only include here a sample plot of the ratio of one unit (Arabia) to the rest of the classes (Fig. 10).

As is easy to see from ratio spectra such as presented in Fig. 10, there are real spectral differences displayed among these units, due to a significant degree of compositional differences. As observed previously for Mars, the variations in spectral shape caused by these compositional differences can be relatively subtle, especially when observed from Earth with a footprint of hundreds of kilometers (e.g., Singer and McCord 1979). Variations in surface physical properties (e.g., particle size, compaction, indura-

tion) can also contribute to observed spectral differences. Compositional and physical variations can have a major effect on the overall albedo of surface units, which in turn has a nonlinear effect on spectral slopes and band depths, complicating interpretation (e.g., Hapke 1981; Clark and Roush 1984). Analysis techniques involving reflectance ratios, scaled (normalized) reflectance, or band depth calculations provide first-order compensation by removing linear aspects of albedo effects. This is often helpful and justified, especially when comparing the spectral shapes of units of similar brightness. When dealing with large differences in brightness, however, the nonlinear effects can be quite significant as a function of wavelength (Geissler 1992). Some of the wavelength-dependent spectral differences observed in our data, such as visible slope differences between high- and low-albedo units, are probably influenced significantly by such effects. Ignoring these effects could lead, for example, to incorrect interpretations of Fe^{3+} content between two units when the main differences might be caused by such factors as variations in opaque phase abundance, particle size, and photometric geometry. Spectral differences (slope, shape, bands) among units with similar albedo can be most confidently attributed to differences in abundance and/or mineralogy of nonopaque phases such as ferric oxides. For these reasons we have limited some of our interpretations to comparisons among units with roughly similar albedo.

We want to remind the reader that in the following discussion the acronyms refer to the spatial areas covered by the corresponding spectral classes shown in Fig. 8, and not only to the geographic areas commonly known by the names from which the acronyms were derived. For example, as we noted before, DR denotes Deucalionis Regio (the region that defined the type spectra for this class) and also part of Noachis which mapped out as the same spectral type (light green class), and SM refers to Sinus Meridiani and all other areas that have similar spectra (red class).

One initial observation is that the depth of the Fe^{3+} absorption band near 0.55 μm varies according to region (as noted from these data by Singer and Miller 1991), implying possible differences in bulk crystalline hematite concentration (although variations in particle size and matrix effects can produce similar differences). In the ratio spectra, the sharper the bend near 0.55 μm, the larger the relative spectral difference due to crystalline hematite between the two regions. Quantitative evaluation of the hematite abundances is difficult because of the strong dependence on particle size and mixing geometry (Morris and Lauer 1990). However, it has been estimated by Singer and Miller (1991) that the differences observed in this data set could be caused by bulk crystalline hematite abundance variations of a few weight percent.

The ratio spectra also show some differences in behavior between about 0.8 and 1.0 μm, which can indicate relative differences in pyroxene abundance and/or composition (e.g., Burns 1970; Adams 1975). Interpretation of some aspects of pyroxene composition based on Fe^{2+} absorptions is difficult from our observations, however, because the data do not extend to long enough wavelengths to define the complete band. An additional complication is the possibility of Fe^{3+} crystal-field absorptions from crystalline ferric oxide minerals, ranging from about 0.86 to about 0.93 μm,

TABLE II
Summary of Spectral Unit Interpretation

Acronym	Type region	Description
SA	Southern Acidalia Planitia	Low albedo, somewhat brighter in the blue but darker in the near-IR than more typical near-equatorial dark regions. Shows least evidence for crystalline hematite (Fe^{3+}) and pyroxene (Fe^{2+}) absorptions shortward of 1 μm.
CL	North Polar Hood	Optically thin and patchy condensate clouds covering northern Acidalia Planitia. Apparent at blue wavelengths but not in red and near-IR.
CY	Chryse Planitia	Relatively high albedo, quite ''red.'' Ratio spectrum of Chryse to Acidalium is smoothly curved, lacks well defined mineral features, implying mineralogic similarity.
AR	Western Arabia	High albedo, greatest VIS slope (''reddest''). Good spectral evidence for crystalline hematite but weaker than for DR.
SM	Meridiani Sinus	Low albedo, shows pyroxene Fe^{2+} band and strong crystalline hematite signature. SM has the strongest bulk hematite signature of all the low-albedo units.
SM2	Meridiani Sinus 2	Low to intermediate albedo, similar spectral shape to SM but with slightly weaker pyroxene and hematite features.
DR	Deucalionis Regio	Intermediate albedo, distinct crystalline hematite signature near 0.55 and 0.86 μm. Appears south of Meridiani Sinus and in part of Noachis. DR has the strongest bulk hematite signature of the high albedo units. Analyzed in detail in Merényi *et al.* 1996.
DR2	Deucalionis Regio 2	Intermediate albedo, variant of DR. Appears north of Meridiani Sinus. Ratio of Arabia to DR2 is nearly a straight line, sloped upwards toward longer wavelengths, suggesting similarities in Fe mineralogy.
L	None	Limb effects, due to observing geometry and/or mixture of surface and sky signals. Not of geologic significance.
S	None	Sky background. Not of geologic significance.
U	None	Unclassified.

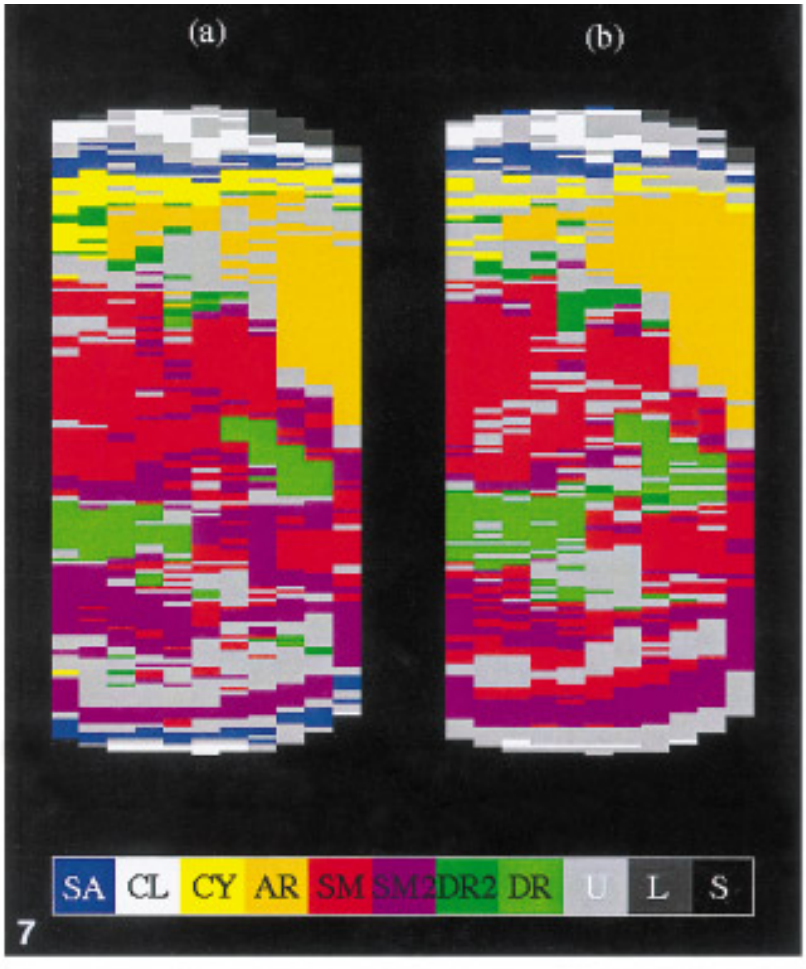
(a)
(b)
SA
CL
CY
AR
SM
SM2
DR2
DR
U
L
S
7

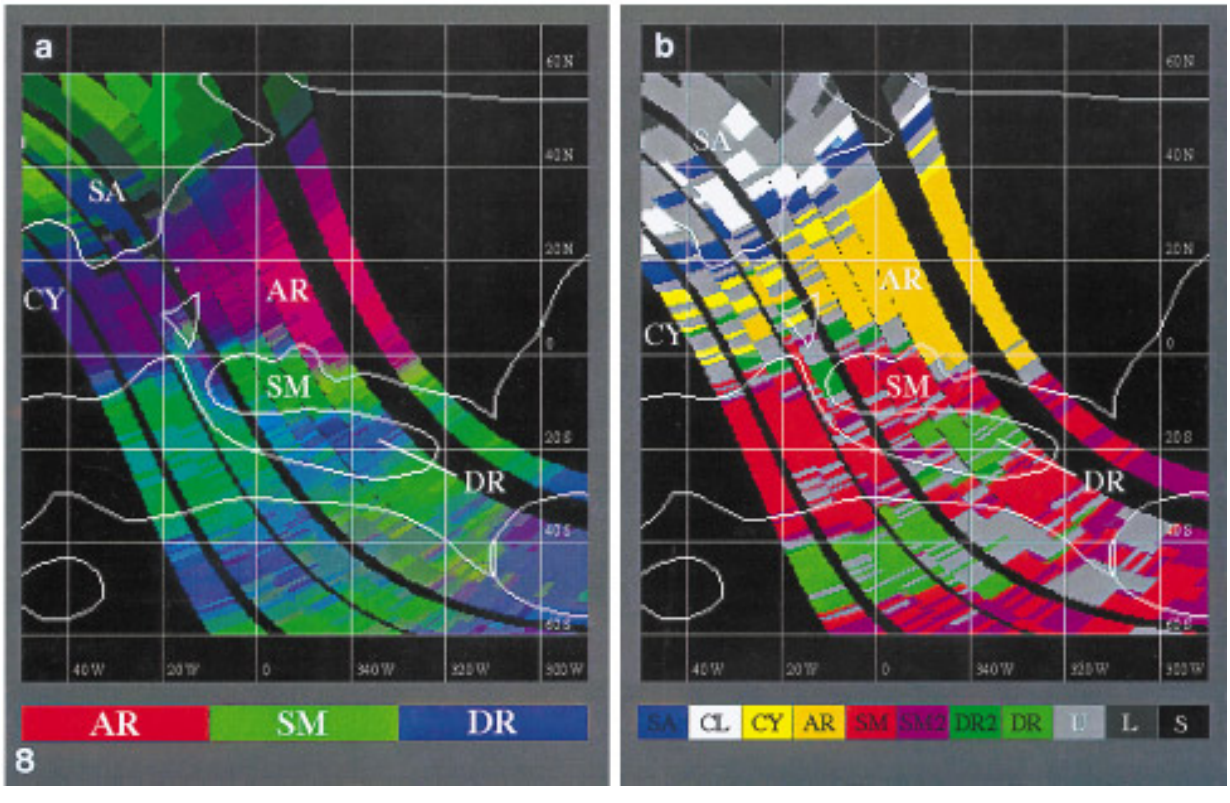
a
b
SA
CY
AR
SM
DR
60 N
40 N
20 N
0
20 S
40 S
60 S
40 W
20 W
0
340 W
320 W
300 W
AR
SM
DR
SA
CL
CY
AR
SM
SM2
DR2
DR
U
L
S
8

depending on composition. Lastly, imperfect correction for telluric water absorptions around 0.82 and 0.94 μm adds ''noise'' to these spectra. We stress that none of these factors affect the evaluation and relative ranking of the classes below. They do, however, complicate specific compositional interpretations.

Our ''high albedo'' units are Arabia (AR), the two Deucalionis units (DR2 and DR), and Chryse (CY), in descending order from peak $r_F = 0.42$ to 0.36 (Table I). Such units are generally interpreted to be rich in fine-grained, heavily oxidized weathering products. Arabia contains some bulk crystalline hematite, based on a 0.55 μm kink and a weak 0.86 μm band, although most of the strong slope from the blue to the near-IR is due to poorly crystalline or nanophase ferric oxide(s), as previously interpreted by various workers (e.g., Evans and Adams, 1979, 1980; Singer, 1982; Morris *et al.* 1989). Arabia is traditionally interpreted as one of the most highly weathered, Fe^{3+}-rich regions on Mars. While our data are consistent with this, we cannot spectrally interpret the weight percent of Fe_2O_3 in Arabia compared with other units. AR and DR2 have nearly identical spectral shapes, differing only in spectral slope. The ratio of Arabia to DR2 in Fig. 10 is nearly linear, with a red continuum slope. The lack of specific bands in the ratio implies that the iron mineralogy of these two regions is similar. The difference in spectral slope might be caused by physical differences affecting scattering, greater Fe^{3+} content in AR in the form of poorly crystalline or nanophase grains, and/or a slightly greater abundance of Fe^{2+}-bearing opaques (such as magnetite, basaltic glass, or basalt fragments) in DR2. These two units are spatially well correlated also; DR2 appears to ''skirt'' AR and SM at locations that were characterized as Dark Red units by Arvidson *et al.* (1989). This has suggested to us the possibility of a genetic relationship as discussed further in Merényi *et al.* (1996). Of these four highest-albedo units DR appears to show the greatest amount of bulk crystalline hematite, based on absorptions near 0.53 and 0.86 μm. Chryse, in contrast, shows the least evidence for crystalline hematite in this group, based on the same spectral criteria. The relationship of these bright units to the globally distributed aeolian dust is not yet clear. The only spectra at these wavelengths for optically thick suspended dust were obtained by McCord *et al.* during the 1973 opposition (1977). While rather low resolution, those data indicate that the aerosol dust has an absorption band minimum centered between 0.86 and 0.90 μm, compared to 0.86 μm for high albedo surface regions observed that year (cf. Huguenin *et al.* 1977). Bell (1992) found a spectral anomaly for Deucalionis in his 0.4–0.8 μm telescopic data. He noticed a steeper negative slope between 0.735 and 0.795 μm for the southern border of Sinus Meridiani/Sinus Sabaeus than within these dark regions. He noted that this anomaly may extend to some of Deucalionis and suggested that it may indicate a more ferrous- or ferric-rich soil than in the surrounding areas.

Our group of ''low albedo'' units consists of Chryse, the two Sinus Meridiani units, SM2 and SM, and South Acidalia (SA), in descending order of r_F from 0.36 to 0.28 (Table I). (As an intermediate albedo unit, Chryse was included in both groups to provide an interpretive link.) Both Chryse and Acidalia show the least indications of bulk crystalline hematite within this group, again based on relative absorption near 0.55 and 0.86 μm (cf. Singer and Miller 1991). SM2 is slightly brighter than SM and has a greater visible slope, consistent with a higher overall content of weathered Fe^{3+}-rich material. While these two units show more crystalline hematite than Chryse and Acidalia, a quantitative comparison between SM and SM2 is difficult. In addition to absorption near 0.86 μm SM has noticeably greater absorption near 0.9 μm. Both Meridiani units show evidence for pyroxenes with band minima around 0.93–0.97 μm, interpreted as an augitic composition with modest Ca and perhaps high Fe (e.g., Singer *et al.* 1990; Miller and Singer 1993). This result is consistent with previous observations and interpretations for near-equatorial dark regions (cf., Singer and McSween 1993; Mustard *et al.* 1993a). The interpretation of pyroxene composition on

FIG. 7. The spectral classes as mapped by the neural network classification. The acronyms are explained in Fig. 6. (a) Classification based on the ratioed spectral image. The training spectra are described in Fig. 6, top row. (b) Classification based on the original, brightness normalized spectral image. The training spectra are shown in Fig. 6, bottom row. Both maps show good agreement (red pixels) with the band depth map on Fig. 3. The network also picks out spectra with weaker bands between 0.8 and 1.02 μm. They are also consistent with the linear mixture model analysis results in Figs. 5 and 8.a. In addtition, further spectral units are distinguished compared to the previous analyses. These are discussed in the text.

FIG. 8. (a) Color composite of three selected endmember fraction images from linear spectral mixture modeling, projected to cylindrical coordinates using the procedure described by Pierazzo and Singer (1993). The endmembers in the mixture model are spectra from South Acidalium (SA), Arabia (AR), Sinus Meridiani (SM), and Deucalionis Regio (DR). This color composite shows the Arabia fraction in red, the Sinus Meridiani fraction in green, and the Deucalionis fraction in blue. (b) Color-coded classification map of the spectral varieties in the 1988 telescopic spectral image. The map was produced by supervised classification of the spectral shapes using an artificial neural network (Fig. 7.b) and then projected into cylindrical coordinates as above. The acronyms of the spectral types are resolved in Fig. 6. Spectral unit interpretation is given in Table II. The fringes at the top of the image may be unreliable due to limb effects.

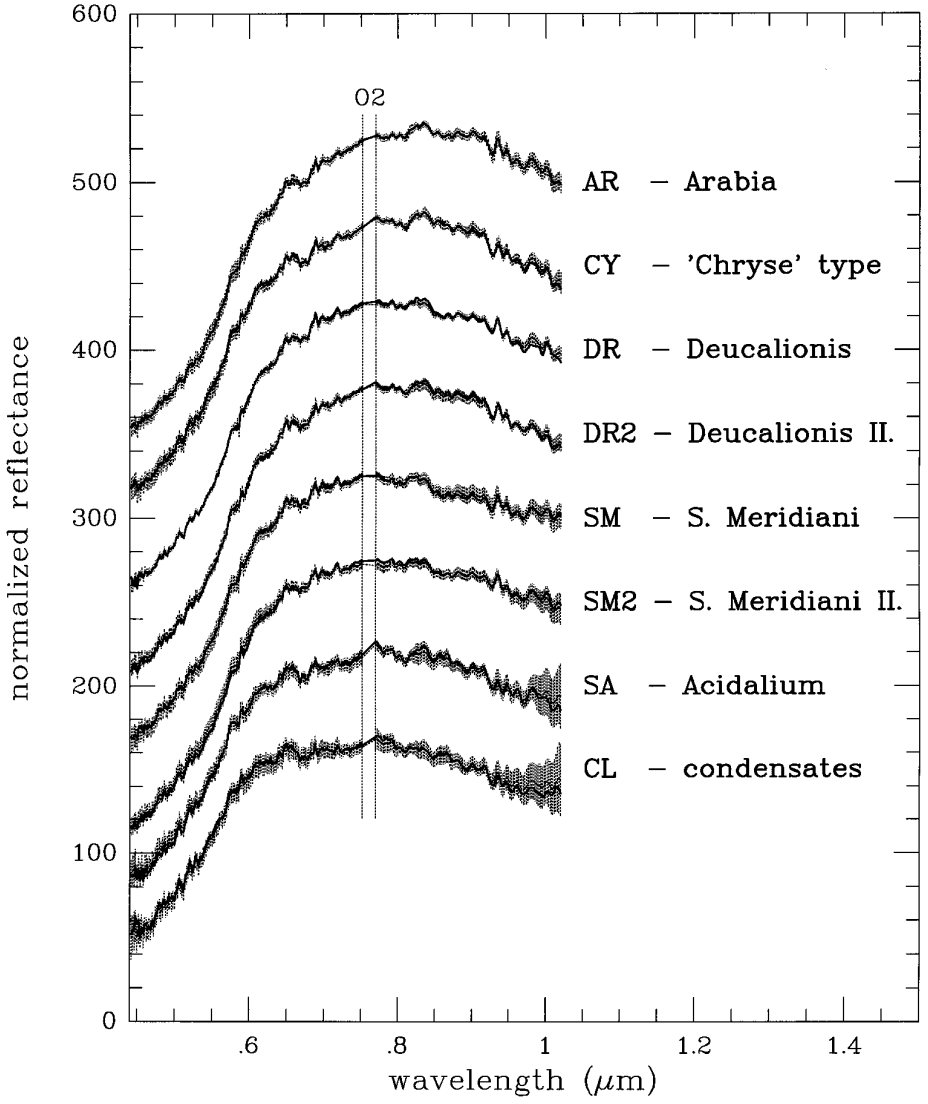

FIG. 9. Comparison of the means of the training spectra with the means of the spectra in the predicted class, for each geologic type. Training means are shown in thick solid lines, class means in thinner dashed lines. The standard deviation of the class spectra for each channel is plotted as an error bar. In most cases, the training and class means are so close to one another that it is hard to distinguish them. The units are arbitrary, the curves are offset for better viewing.

Mars is complicated by the closeness of crystalline ferric oxide bands, which range from 0.86 μm for hematite to longward of 0.9 μm for other phases (e.g., Sherman *et al.* 1982). Relative to SM2, the absorption near 0.9 μm seen for SM could be attributed either to a second crystalline ferric oxide, such as goethite (FeOOH), a Ca- and Fe-poor pyroxene, or some combination of ferric oxide(s) and pyroxene(s). Similar questions have arisen from Phobos 2 ISM spectral data for other regions on Mars (e.g., Geissler *et al.* 1993; Murchie *et al.* 1993b) and from laboratory studies (e.g., Morris *et al.* 1994) and remain unanswered. Acidalia is distinctly different from SM and SM2 longward of about 0.9 μm. Acidalia shows no indications of a pyroxene band minimum between 0.9 and 1.0 μm, but the reflectance is steadily decreasing out to the end of our data (near 1.02 μm). This could be consistent with an abundant high-Ca pyroxene and/or olivine, mafic glass, or perhaps it is a broad negative slope effect due to coatings or other physical factors (Singer and Roush 1983; Fischer *et al.* 1991). High quality spectra extending further into the near infrared are required to resolve this.

That there appears to be a significant correlation between low-albedo units and bulk crystalline hematite is not unreasonable. Earlier work by Soderblom *et al.* (1978) and McCord *et al.* (1982) first pointed to this possibility. Bulk crystalline hematite is more stable at higher tempera-

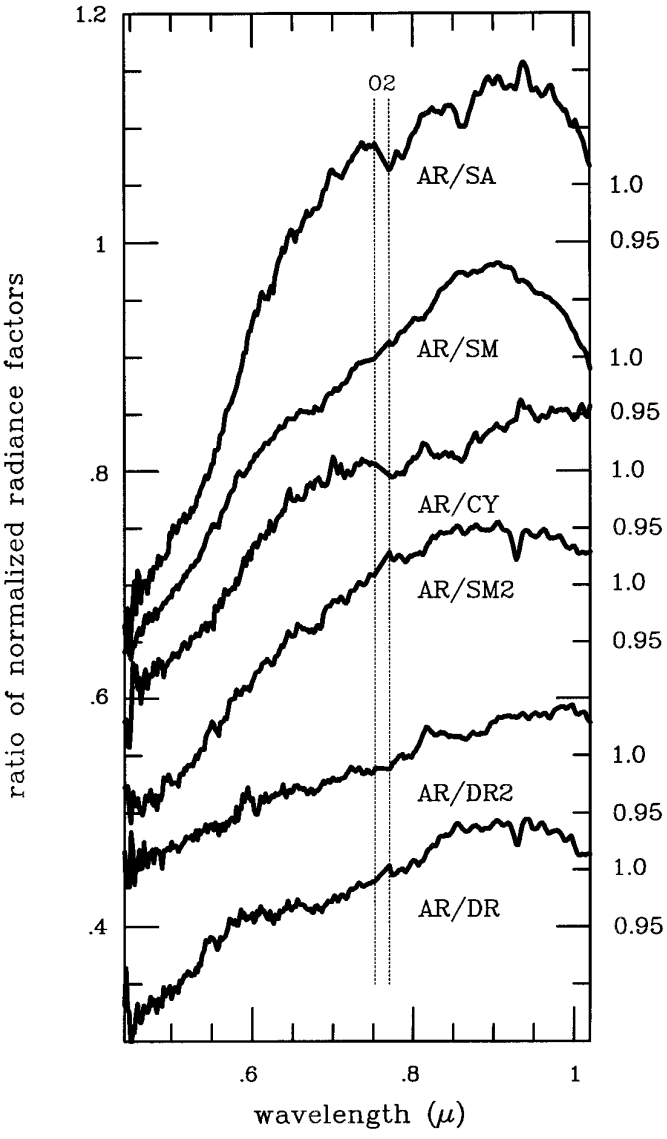

FIG. 10. The ratio of the mean of the Arabia type (AR) class to the class means of the other study regions. The curves are offset for clarity. A concave upward inflection near 0.55 μm indicates a stronger hematite absorption in the denumerator (i.e., Arabia has a stronger hematite signature than all other regions except for DR).

tures than other ferric oxides and oxyhydroxides, and can form from the thermal metamorphism of the later. Gooding (1978) concluded that hematite should be the most stable iron-bearing phase under current martian conditions. Bulk crystalline hematite can also form directly as a high-temperature alteration product associated with volcanic activity and impact cratering. As such its association with basaltic highland material on Mars should not be surprising. Finally, an interesting possibility pointed out by Singer *et al.* (1993) is that there appears to be a consistent trend that, independent of albedo, surface units in the younger northern lowlands contain less crystalline hematite than those on the highland terrains. Our units Arabia, Sinus Meridiani, SM2, and most occurrences of DR are on highlands; South Acidalia and Chryse occur on lowlands. This is among the first evidence for any compositional (spectral) difference which correlates with the global geologic crustal dichotomy on Mars, although we cannot yet draw any conclusions concerning the relationship of the two. We recommend that this issue receive particular attention during future observations of the planet.

4.2. Geologic Interpretation

The geologic interpretation of the spectral units mapped in Figs. 7 and 8 is summarized in Table II.

5. CONCLUSIONS

Two independent analyses of a visible/near-infrared telescopic spectral image of Mars obtained during the 1988 opposition indicate that geologically significant spectral variations can be detected beyond the small number of Viking color units commonly used to characterize the Martian surface. The use of advanced mathematical methods facilitated the exploitation of subtle spectral variations in very high-dimensional spectral data.

With linear mixture modeling (Adams *et al.* 1986), we established four major spectral endmembers for our scene along with their relative abundances, which generally fit well with earlier analyses. Using a nonlinear artificial neural network classification method, we have been able to separate further spectral units that are too similar for linear inversion methods. Examples of such pairs of spectrally similar units are optically thin condensates over the north polar hood and South Acidalia; and Deucalionis Regio and its variant, DR2, in which the subtle spectral distinction is relevant in terms of the geological interpretation.

An important result is the discovery of the spectral distinction of the equatorial classical albedo feature Deucalionis Regio. Consequent work (Merényi *et al.* 1996) has shown since that its soil properties are different from the materials in nearby regions such as Arabia, Acidalium, Meridiani, and probably Oxia.

Comparison of the spectral classes also reveals evidence for a tendency in iron composition that corresponds to the global crustal dichotomy of Mars: the younger northern lowlands show less evidence for bulk crystalline hematite than the southern highlands.

ACKNOWLEDGMENTS

We thank J. B. Adams and M. O. Smith for providing the linear mixture model software. We appreciate careful and stimulating reviews by J. F. Bell III and J. F. Mustard. We also thank J. F. Bell III for lending us his data for comparison. For spectral classification, the artificial neural network simulation package "NeuralWorks Professional II," by NeuralWare, Inc., was used. This project was partially supported by NASA

Grant NAGW-1059 and by the University of Arizona Planetary Image Research Laboratory. The computing facilities of the Lunar and Planetary Laboratory and the Planetary Image Research Laboratory at the University of Arizona and the Khoros image processing package (Rasure and Young 1992) were used for the image analysis work.

REFERENCES

Adams, J. B. 1975. Interpretation of visible and near-infrared diffuse reflectance spectra of pyroxenes and other rock-forming minerals. *Infrared and Raman Spectroscopy of Lunar and Terrestrial Minerals*, (C. Carr, Jr., Ed.), pp. 91–116. Academic Press, San Diego.

Adams, J. B., M. O. Smith, and P. E. Johnson 1986. Spectral mixture modeling: A new analysis of rock and soil types at the Viking Lander 1 site. *J. Geophys. Res.* **91,** 8098–8112.

Antoniadi, E. M. 1930. *La Planète Mars*. Hermann, Paris.

Arvidson, R. E., E. A. Guiness, M. A. Dale-Bannister, J. B. Adams, M. O. Smith, P. R. Christensen, and R. B. Singer 1989. Nature and distribution of surficial deposits in Chryse Planitia and vicinity, Mars. *J. Geophys. Res.* **94,** 1573–1587.

Bell, J. F., III, P. G. Lucey, and T. B. McCord 1992. Charge-coupled device imaging spectroscopy of Mars. 1. Instrumentation and data reduction/analysis procedures. *Exper. Astron.* **2,** 287–306.

Bell, J. F. III 1992. Charge-coupled device imaging spectroscopy of Mars. 2. Results and implications for martian ferric mineralogy. *Icarus* **100,** 575–597.

Benediktsson, J. A., P. H. Swain, O. K. Ersoy, and D. Hong 1990. Classification of very high dimensional data using neural networks. In *IGARSS'90 10th Annual International Geoscience and Remote Sensing Sympos*., Vol. 2, p. 1269.

Blount, G., M. O. Smith, J. B. Adams, R. Greeley, and P. R. Christensen 1990. Regional aeolian dynamics and sand mixing in the Gran Desierto: Evidence from Landsat Thematic Mapper images. *J. Geophys. Res.* **95,** 15,463–15,482.

Boardman, J. W. 1993. Automating spectral unmixing of AVIRIS data using convex geometry concepts. In *Proc. Fourth Airborne Geoscience Workshop, Washington, D.C., Oct. 25–29*, Vol. 1, pp. 11–14. JPL Publication 93-26, 1993.

Burns, R. G. 1970. *Mineralogical Applications of Crystal Field Theory*. Cambridge Univ. Press, Cambridge, UK.

Clark, R. N., and T. L. Roush, 1984. Reflectance spectroscopy: Quantitative analysis techniques for remote sensing applications. *J. Geophys. Res.* **89,** 6329–6340.

Clark, R. N., G. A. Swayze, R. B. Singer, and J. Pollack 1990. High resolution spectra of Mars in the 2.3 μm region: Evidence for the mineral scapolite. *J. Geophys. Res. Planets* **95,** 14,463–14,479.

Evans, D. L., and J. B. Adams 1979. Comparison of Viking Lander multispectral images and laboratory reflectance spectra of terrestrial samples. *Lunar Planet. Sci.* **10,** 1829–1834.

Evans, D. L., and J. B. Adams 1980. Amorphous gels as possible analogs to martian weathering products. *Lunar Planet. Sci.* **11,** 757–763.

Farrand, W. H., and R. B. Singer 1991. Analysis and mapping of palagonite tuffs of Pavant Butte, Millard County, Utah. *J. Geophys. Res. Lett.* **18,** No. 12, 2237–2240.

Fischer, E. M., C. M. Pieters, and S. F. Pratt 1991. The perplexing continuum slope of Mars: Effects of thin ferric coatings and viewing geometry. *Lunar Planet. Sci.* **22,** 381-382. [Abstract]

Geissler, P. E. 1992. *Spectrophotometric Mapping of Coprates Quadrangle, Mars*. Ph.D. Thesis, University of Arizona, Tucson.

Geissler, P. E., R. B. Singer, G. Komatsu, S. Murchie, and J. F. Mustard 1993. An unusual spectral unit in west Candor Chasma: Evidence for aquaeous or hydrothermal alteration in the martian canyons. *Icarus* **106,** 380–391.

Hapke, B., and E. Wells 1981. Bidirectional reflectance spectroscopy. 1. Theory. *J. Geophys. Res.* **86,** 3,039–3,054.

Head, J. N., R. B. Singer, and P. E. Geissler 1992. Multispectral Study of Cerberus Dark Materials. *Lunar Planet. Sci.* **23,** 509–510. [Abstract]

Hepner, G. F., T. Logan, N. Ritter, andN. Bryant 1990. Artificial neural network classification using a minimal training set: Comparison to conventional supervised classification. *Photogrammetric Eng. Remote Sensing* **56,** No. 4, 469–473.

Howell, E. S., E. Merényi, and L. A. Lebofsky 1994. Classification of asteroid spectra using a neural network *J. Geophys. Res. Planets* **99,** No. E5, 10,847–10,865.

Huang, W., and R. Lippman 1987. Comparisons between neural net and conventional classifiers. In *IEEE First International Conference on Neural Networks*, Vol. 4, pp. 485–494. San Diego.

Huguenin, R. L., J. B. Adams, and T. B. McCord 1977. Mars: Surface mineralogy from reflectance spectra. *Lunar Sci.* **8,** 478–480.

Gooding, J. L. 1978. Chemical weathering on Mars: Thermodynamic stabilities of primary minerals (and their alteration products) from mafic igneous rocks. *Icarus* **33,** 483–513.

Kohonen, T. 1988. *Self-Organization and Associative Memory*. Springer-Verlag, New York.

McCord, T. B., R. L. Huguenin, D. Mink, and C. M. Pieters 1977. Spectral reflectance of martian areas during the 1973 opposition: Photoelectric filter photometry 0.33–1.10 μm. *Icarus* **31,** 25–39.

McCord, T. B., R. B. Singer, B. R. Hawke, J. B. Adams, D. L. Evans, J. W. Head, P. J. Mouginis-Mark, C. M. Pieters, R. L. Huguenin, and S. H. Zisk 1982. Mars: Definition and characterization of global surface units with emphasis on composition. *J. Geophys. Res.* **87,** 10,129–10,148.

Merényi, E., K. S. Edgett, and R. B. Singer 1993a. Deucalionis Regio, Mars: Evidence for a unique mineralogic endmember and a crusted surface. *Lunar Planet. Sci.* **24,** 979. [Abstract]

Merényi, E., R. B. Singer, and W. H. Farrand 1993b. Classification of the LCVF AVIRIS test site with a Kohonen artificial neural network. In *Proc. Fourth Airborne Geoscience Workshop, Washington, D.C., Oct. 25–29,* Vol. 1, pp. 117–120. JPL Publication 93-26, 1993.

Merényi, E., K. S. Edgett, and R. B. Singer 1996. Deucalionis Regio, Mars: Evidence for a new type of immobile weathered soil unit. *Icarus* **124,** 296–307.

Miller, J. S., R. B. Singer, W. K. Wells, and L. Weller 1992. Radiance factor calibration of 1988 visible and near IR spectral images of Mars. *Lunar Planet. Sci.* **23,** 911–912. [Abstract]

Miller, J. S., and R. B. Singer 1993. Analysis of pyroxene absorptions observed in martian dark regions. *Lunar Planet. Sci.* **24,** 989–990. [Abstract]

Morris, R. V., D. G. Agresti, H. C. Lauer, Jr., J. A. Newcomb, T. D. Shelfer, and A. V. Murali, 1989. Evidence for pigmentary hematite on Mars based on optical magnetic, and Mossbauer studies of super-paramagnetic (nanocrystalline) hematite. *J. Geophys. Res.* **94,** 2760–2778.

Morris, R. V., and H. V. Lauer 1990. Matrix effects for reflectivity spectra of dispersed nanophase (superparamagnetic) hematite with application to martian spectral data. *J. Geophys. Res.* **95,** 5101–5109.

Morris, R. V., D. C. Golden, J. F. Bell, III, andH. V. Lauer Jr. 1994. Hematite, pyroxene, and phyllosilicates on Mars: Implications from oxidized impact melt rocks from Manicouganan Crater, Quebec, Canada. *J. Geophys. Res.* **100,** 5319–5328.

MURCHIE, S., J. F. MUSTARD, S. ERARD, P. GEISSLER, AND R. B. SINGER 1993a. Variations in the Fe mineralogy of bright martian soil. *Lunar Planet. Sci.* **24,** 1029–1030. [Abstract]

MURCHIE, S. L., J. F. MUSTARD, J. L. BISHOP, J. W. HEAD, C. M. PIETERS, AND S. ERARD 1993b. Spatial variations in the spectral properties of bright regions on Mars. *Icarus* **105,** 454–468.

MUSTARD, J. F., S. ERARD, J. P. BIBRING, J. W. HEAD, S. HURTREZ, Y. LANGEVIN, C. M. PIETERS, AND C. J. SOTIN 1993a. The surface of Syrtis Major: Composition of the volcanic substrate and mixing with altered dust and soil. *J. Geophys. Res.* **98,** 3387–3400.

MUSTARD, J. F., S. L. MURCHIE, AND S. ERARD, 1993b. Composition of weakly altered martian crust. *Lunar Planet. Sci.* **24,** 1039–1040. [Abstract]

MUSTARD, J. F. 1993. Relationship of soil, grass and bedrock over the Kaweah serpentine melange through spectral mixture analysis of AVIRIS data. *Remote Sens. Environ.* **44,** 293–308.

NEURALWARE, INC. 1991. Neural Computing. In *NeuralWorks Professional II Manuals* NC, p. 317.

NINOMIYA, Y., AND I. SATO 1990. Estimation of SiO_2 content using thermal infrared reflectance spectra of rocks. In *Proc. 10th Annual Int'l Geosci. and Remote Sensing Symposium*, Vol. 2, p. 979.

PAO, Y. H. 1989. *Adaptive Pattern Recognition and Neural Networks*. Addison–Wesley, Reading, MA.

PIERAZZO, E., AND R. B. SINGER 1993. Wavelength dependence of limb-darkening of Mars from visible and near-IR telescopic spectral imaging. *Lunar Planet. Sci.* **24,** 1139–1140. [Abstract]

PINET, P., AND S. CHEVREL 1990. Spectral identification of geological units on the surface of Mars related to the presence of silicates from Earth-based near-infrared telescopic charge-coupled device imaging. *J. Geophys. Res.* **95,** 14,435–14,446.

PINET, P. C., S. D. CHEVREL, AND P. MARTIN 1993. Copernicus: A regional probe of the lunar interior. *Science* **260,** 797–801.

RASURE, J., AND M. YOUNG 1992. An open environment for image processing software development. *Proceedings of the SPIE/IS&T Symposium in Electronic Imaging, February 14, 1992*, Vol. 1659.

ROUSH, T. L., D. L. BLANEY, AND R. B. SINGER, 1993. The surface composition of Mars as inferred from spectroscopic observations. In *Remote Geochemical Analysis: Elemental and Mineralogical Composition* (C. M. Pieters and P. A. J. Englert, Eds.), pp. 367–393.

RYAN, T. W., P. J. SEMENTILLI, P. YUEN, AND B. R. HUNT 1991. Extraction of shoreline features by neural nets and image processing. *Photogrammetric Eng. Remote Sensing* **57,** 7,947–7,955.

SHERMAN, D. M., R. G. BURNS, AND V. M. BURNS 1982. Spectral characteristics of the iron oxides with application to the martian bright region mineralogy. *J. Geophys. Res.* **87,** 10,169–10,180.

SINGER, R. B., AND T. B. MCCORD 1979. Mars: Large scale mixing of bright and dark materials and implications for analysis of spectral reflectance. *Lunar Planet. Sci.* **10,** 1825–1848.

SINGER, R. B. 1982. Spectral evidence for the mineralogy of high-albedo soils and dust on Mars. *J. Geophys. Res.* **87,** 10,159–10,168.

SINGER, R. B., AND T. L. ROUSH 1983. Spectral reflectance properties of particulate weathered coatings on rocks: Laboratory modeling and applicability to Mars. *Lunar Planet. Sci.* **24,** 708–709. [Abstract]

SINGER, R. B., J. S. MILLER, K. W. WELLS, AND E. S. BUS 1990. Visible and near-IR spectral imaging of Mars during the 1988 opposition. *Lunar Planet. Sci.* **21,** 1164–1165. [Abstract]

SINGER, R. B., AND J. S. MILLER 1991. "Evidence for crystalline hematite as an accessory phase in martian soils." In *Workshop on the Mars Surface and Atmosphere Through Time* (R. M. Haberle, Ed.), pp. 134–135. LPI Tech. Rept. 92-02, Lunar and Planetary Institute, Houston.

SINGER, R. B., AND H. Y. MCSWEEN 1993. The composition of the igneous martian crust: Evidence from remote sensing and SNC meteorites. In *Resources of Near-Earth Space* (J. Lewis, M. S. Matthews, and M. L. Guerrieri, Eds.), pp. 709–736. Univ. of Arizona Press, Tucson.

SINGER, R. B., J. S. MILLER, AND E. MERÉNYI 1993. Evidence for a global compositional dichotomy on Mars. *Bull. Amer. Astron. Soc.* **25,** 1032. [Abstract]

SMITH, M. O., S. L. USTIN, J. B. ADAMS, AND A. R. GILLESPIE 1990. Vegetation in deserts. 1. A regional measure of abundance from multispectral images. *Remote Sensing Environment* **31,** 1–26.

SODERBLOM, L. A., E. EDWARDS, E. M. ELIASON, E. M. SANCHEZ, AND M. P. CHARETTE 1978. Global color variations on the martian surface. *Icarus* **34,** 446–464.

SODERBLOM, L. A. 1992. The composition and mineralogy of the martian surface from spectroscopic observations: 0.3 μm to 50 μm. In *Mars* (H. H. Kieffer, B. M. Jakosky, C. W. Snyder, and M. S. Matthews, Eds.), pp. 557–593.

TODY, D. 1986. The IRAF data reduction and analysis system. *Proc. SPIE Instrum. Astron.* **6,** 627, 733.

TOMPKINS, S., J. F. MUSTARD, C. M. PIETERS, AND D. W. FORSYTH 1993. Objective determination of image end-members in spectral mixture analysis of AVIRIS data. In *Proc. Fourth Airborne Geoscience Workshop, Washington, D.C., Oct. 25–29*, Vol. 1, pp. 177–180. JPL Publication 93-26, 1993.